IOP Publishing Superconductor Science and Technology
Supercond. Sci. Technol. **35** (2022) 125011 (16pp) https://doi.org/10.1088/1361-6668/ac9f82

An initial magnet experiment using high-temperature superconducting STAR® wires

Xiaorong Wang[1,*], Timothy J Bogdanof[1], Paolo Ferracin[1], William B Ghiorso[1], Stephen A Gourlay[1], Hugh C Higley[1], Janakiram Kaushal Kadiyala[2], Soumen Kar[2], Reginald Lee[1], Linqing Luo[1], Maxwell A Maruszewski[1], Robert Memmo[1], Cory S Myers[1], Soren O Prestemon[1], Jithin Sai Sandra[2], Venkat Selvamanickam[3], Reed Teyber[1], Marcos Turqueti[1] and Yuxin Wu[1]

[1] Lawrence Berkeley National Laboratory, Berkeley, CA 94720, United States of America
[2] AMPeers LLC, Houston, TX 77059, United States of America
[3] Department of Mechanical Engineering, Advanced Manufacturing Institute, Texas Center for Superconductivity, University of Houston, Houston, TX 77204, United States of America

E-mail: xrwang@lbl.gov

Received 21 August 2022, revised 20 October 2022
Accepted for publication 2 November 2022
Published 14 November 2022

Abstract

A dipole magnet generating 20 T and beyond will require high-temperature superconductors such as $Bi_2Sr_2CaCu_2O_{8-x}$ and $REBa_2Cu_3O_{7-x}$ (RE = rare earth, REBCO). Symmetric tape round (STAR®) wires based on REBCO tapes are emerging as a potential conductor for such a magnet, demonstrating a whole-conductor current density of 580 A mm^{-2} at 20 T, 4.2 K, and at a bend radius of 15 mm. There are, however, few magnet developments using STAR® wires. Here we report a subscale canted cosθ dipole magnet as an initial experiment for two purposes: to evaluate the conductor performance in a magnet configuration and to start developing the magnet technology, leveraging the small bend radius afforded by STAR® wires. The magnet was wound with two STAR® wires, electrically in parallel and without transposition. We tested the magnet at 77 and 4.2 K. The magnet reached a peak current of 8.9 kA, 78% of the short-sample prediction at 4.2 K, and a whole-conductor current density of 1500 A mm^{-2}. The experiment demonstrated a minimum viable concept for dipole magnet applications using STAR® wires. The results also allowed us to identify further development needs for STAR® conductors and associated magnet technology to enable high-field REBCO magnets.

Keywords: REBCO, magnet, STAR®

(Some figures may appear in colour only in the online journal)

1. Introduction

Recent progress of multi-tape high-current $REBa_2Cu_3O_{7-\delta}$ (REBCO, RE = rare earth elements) cable paves a way toward high-field accelerator magnets that can generate a dipole field beyond 16 T, the perceived limit for the state-of-art Nb_3Sn magnet technology [1]. Two European programs, EuCARD and EuCARD2 [2, 3], have successfully demonstrated record dipole fields of 5.4 T at 4.2 K using a twin-tape cable [4–6] and 4.5 T using a Roebel cable [6–8]. Both cables can be characterized as a stacked-tape architecture that is ubiquitous in various REBCO-based fusion cable concepts [9, 10].

A round conductor, such as the Conductor on Round Core (CORC®) wire [11–14], represents an alternative architecture for a multi-tape REBCO cable. With highly-aspected REBCO

* Author to whom any correspondence should be addressed.

tapes helically wrapped around a round former, the resulting conductor becomes mechanically and magnetically isotropic, a desirable feature to develop high-field accelerator magnets that require tight conductor bending. The U.S. Magnet Development Program (MDP) [15, 16], sponsored by the Office of High Energy Physics at the Department of Energy, is pursuing several magnet concepts using CORC® conductors [17–19].

The Symmetric Tape Round (STAR®) wire is another quintessential multi-tape round REBCO conductor [20–23]. Although its fundamental geometry is similar to CORC® conductors, the STAR® wire pushes the concept further with several distinctions. The thin substrate, 15–22 μm thick, and Cu of asymmetric thickness at each side of the tape, position the REBCO layer near the neutral axis of the composite tape, improving the tape bending performance [21, 23, 24]. STAR® wires not only can use a Cu former as small as 0.7 mm diameter but also usually contain less than 15 REBCO tapes. As a result, STAR® wires have a diameter less than 3 mm and a minimum bend radius of 15 mm. A whole-conductor current density of 580 A mm^{-2} at 20 T, 4.2 K is also demonstrated [25].

Although the performance of STAR® wire progressed significantly in the past few years, there are few reports on using STAR® wires in magnets [24]. Here we report the fabrication and test of a subscale canted cosθ (CCT) dipole magnet called s0. The 50 mm aperture magnet has two layers and three turns of conductors in each layer. Each layer has two STAR® wires that are electrically in parallel, without transposition. We assembled both layers into the s0 magnet and tested it at 77 and 4.2 K. The magnet reached a peak current of 8.9 kA, 78% of the short-sample prediction, and a whole-conductor current density of 1500 A mm^{-2}.

With this initial experiment of magnet development using STAR® wires, we intend to start addressing the following questions: How to make a high-field dipole magnet with STAR® wires? What is the magnet and conductor performance? What further developments are needed for the magnet and conductor technology to enable a dipole field of 20 T and above?

We describe the magnet design and fabrication in section 2, followed by the details of measurement setup and protocol in section 3. Sections 4 and 5 present the test results at 77 and 4.2 K. Section 6 presents the ramp-rate dependence of the current distribution, followed by the electrical-joint performance in section 7. Finally, we discuss the implications of s0 magnet and further development needs for high-field dipole magnets based on STAR® wires.

Compared to the earlier work on CCT magnets using CORC® conductors, this work introduced the ribbon-like conductor configuration of two STAR® wires and the associated coil fabrication details, including a semi-automated winding method and a concept of electrical termination for multiple STAR® wires. We also measured and discussed current distribution between the two electrically-parallel wires, which can be important for further development and application of high-current cables consisting of multiple compact STAR® wires in high-field magnets.

The experiment of the s0 magnet suggested that it is possible to transfer the exemplary performance of STAR® wires from short samples to magnets. We expect the continued development to bring more conductor and technology options to enable high-field REBCO magnets for high-energy physics and fusion applications.

2. Design and fabrication of s0

2.1. Magnet configuration

The s0 magnet follows a two-layer CCT dipole design. The CCT concept was introduced by Meyer and Flasck in [26]. Since then, various authors have further developed and demonstrated the concept [27–40]. The MDP is developing high-field CCT dipole magnet technology for Nb_3Sn [41–43] and two high-temperature superconductors: $Bi_2Sr_2CaCu_2O_{8+x}$ [44–47] and REBCO [19, 48, 49].

Figure 1 shows the magnet configuration. To leverage the small wire diameter and boost the total magnet current, each layer has two STAR® wires that are electrically in parallel. After winding, the wires essentially formed a ribbon-type cable with no wire transposition. Table 1 lists the main parameters for the magnet.

Figure 2 shows the Cartesian coordinate system of the s0 magnet. It also shows the conductor groove that is normal to the cylindrical surface of the mandrel.

We describe the longitudinal axis of each wire using a parametric equation for a CCT dipole [37]. The axis of Wire 1 follows

$$\begin{aligned} x_1 &= r_1 \cos t, \\ y_1 &= r_1 \sin t, \\ z_1 &= \frac{r_1 \sin t}{\tan \alpha_1} + p_1 t, \end{aligned} \tag{1}$$

where x_1, y_1, z_1 are the coordinates of the wire axis as a function of parameter t; r_1 is the radius of the longitudinal axis of Wire 1 when projected to the x–y plane; α_1 is the wire tilt angle between the longitudinal axis of the wire, when projected to the y–z plane, and the z axis. Over a period of 2π for the parameter t, the wire progresses along the z axis by $2\pi p_1$.

Suppose the groove contains a single stack of identical wires, we show that every wire follows (1) with a specific radius and tilt angle. If each wire is in contact with its neighboring wire(s), then the radius of the longitudinal axis of Wire n, when projected to the x–y plane, can be given by $r_n = r_1 + d(n-1)$ where d is the wire diameter.

When we machine the groove in a mandrel, the end mill is normal to the cylindrical surface of the mandrel. This has two implications. First, all the wires in the groove have identical z at any parameter t, $z_1(t) = z_n(t)$. Second, all the wires have the same pitch, $p_1 = p_n$. Therefore, using (1), we can relate the tilt angle of Wire n to that of Wire 1 by $\tan\alpha_n / \tan\alpha_1 = r_n / r_1$. As r_n increases, the tilt angle α_n for Wire n also increases (figure 2).

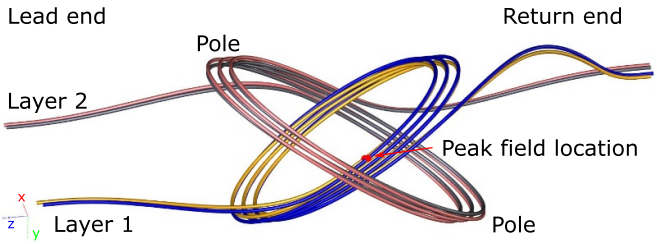

Figure 1. Sketch of the s0 coil winding. Layer 1 is the inner layer and Layer 2 is the outer layer. Each layer has two wires: Wire 1 is the inner one closer to the magnet aperture; Wire 2 is the outer one next to the mandrel surface. The current enters and leaves the magnet from the lead end. The wires from both layers meet at the return end to form the inter-layer joint. The red dots show the locations of the highest magnetic field that is transverse to the longitudinal axes of the wires in the s0 magnet.

Table 1. Main design parameters for the s0 magnet. The transfer function of the magnetic fields assumes an even current distribution between the both wires of each layer.

		CCT layer	
Design parameters	Unit	1	2
Inner diameter (ID)	mm	50.00	64.40
Outer diameter (OD)	mm	62.40	76.80
Mandrel length	mm	274	
Mandrel material	—	Al alloy 6061-T6	
Number of turns in each layer	—	3	
Length of a single wire inside each mandrel	m	1.1	1.2
Groove diameter/depth	mm	2.10/4.18	
Mandrel rib thickness at the mid-plane	mm	1.0	
Wire tilt angle at the mid-plane	degree	33	−33
Minimum bend radius of the wire center line	mm	15.4	18.2
Termination length	mm	127	
Termination OD	mm	7.94	
Aperture dipole-field transfer function	T kA^{-1}	0.049	0.039
Peak conductor-field transfer function	T kA^{-1}	0.406	0.369
Magnet inductance	μH	0.24	

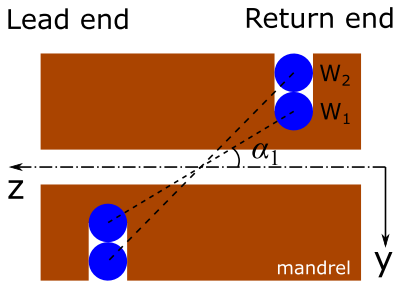

Figure 2. The Cartesian coordinate system for Layer 1 of the s0 magnet, with only the y and z axes shown. The z axis is the rotational axis of the cylindrical mandrel. The y–z plane cuts through the pole regions of the magnet; the cross sections of the wires on the y–z plane are circles. The x–z plane is the mid-plane of the magnet.

2.2. STAR® conductor

In March 2019, AMPeers LLC provided five STAR® wires to develop the s0 magnet. Each 2 m long wire contains eight layers of REBCO tapes wrapped around a 0.81 mm diameter Cu former. Each layer has one tape. AMPeers produced the REBCO tapes with 15–22 μm thick substrates. The Cu stabilizer, with a thickness ranging from 18–30 μm, is electroplated primarily on the REBCO side such that the REBCO layer is closer to the neutral plane of the final tape. Wider tapes are used in the outer layers of the wire: the tape width increases from 1.8 mm of the inner first two layers to 2.6 mm of the outermost two layers.

The wires have a nominal outer diameter of 1.9 mm and a minimum bend radius of 15 mm. The ratio of Cu to non-Cu material is 0.51, taking into account the Cu former and Cu stabilizer in each REBCO tape. The wires do not have electrical insulation. The wires are described as Wires #2 to #6 in [24] that has more details on the wires.

2.3. Magnet fabrication

The magnet mandrels were made of aluminum alloy 6061-T6. To electrically insulate the mandrels from the STAR® wires, we anodized the mandrels with a 50 μm thick coating and sealed with Teflon® according to the MIL-A-8625 F Type-III standard. Anodized aluminum mandrels were also used in CCT magnets wound with NbTi conductors [38, 50, 51].

Making one coil consisted of the following steps. Using a semi-automated winding table, we wound one wire into the empty groove. The wire remained at the bottom of the groove under a winding tension of 10 N. The next wire was then wound on top of the previous one, under the same winding

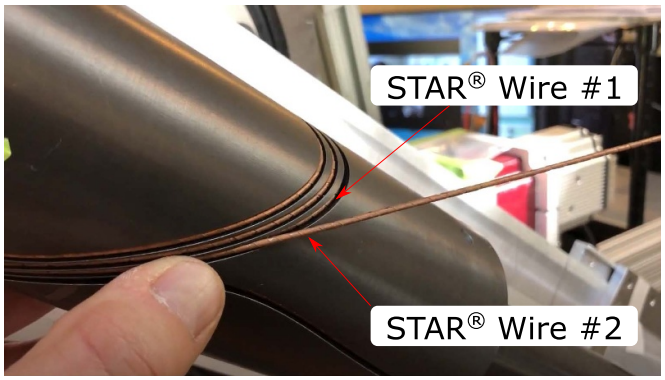

Figure 3. Winding the second STAR® wire in Layer 2 using a semi-automated winding table. The first STAR® wire is in the groove. The development of the winding table was inspired by a video from Glyn Kirby on an automated winding machine [52]. Here is a youtube video showing the winding process.

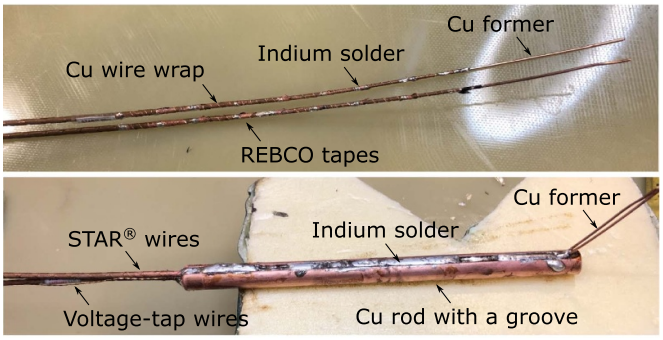

Figure 4. Top: STAR® wires with the prepared ends. Bottom: the finished termination with both STAR® wires placed in the groove of a Cu rod.

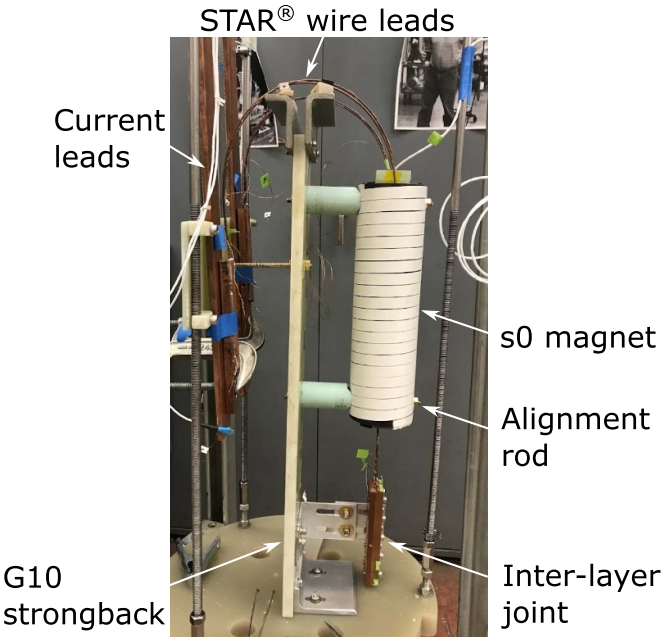

Figure 5. The s0 magnet attached to the test stand.

tension. Figure 3 and the video show the winding of the second wire for Layer 2. A pair of twisted voltage-tap wires was then wound into the groove and stayed next to the STAR® wires.

We also co-wound a single-mode optic fiber into Layer 2 after the voltage-tap wires were installed, following the same procedure and tension as used in co-winding the voltage-tap wires. The polyimide-coated optical fiber has a diameter of 175 μm, fitting in the space between the wall of the radial groove and the STAR® wire as a result of the winding tension.

The coils were not impregnated. We wrapped an adhesive electric tape around the completed layer to constrain the conductors and instrumentation wires. The electrical resistance between the STAR® wires and mandrel was higher than 60 MΩ after winding.

The electrical termination was made in two steps.

We first prepared the wire end by tapering and exposing the REBCO tapes, similar to what is reported by Mulder *et al* [53]. We wrapped around the tapes using a 0.127 mm diameter fine Cu wire to hold the tapes around the Cu former. Then, we soldered the tape ends to the wire using a minimum amount of indium (figure 4).

Second, we placed the prepared wire ends into the groove machined in a Cu rod, together with the voltage-tap wires. We sealed the open end of the groove with an aluminum foil. Indium strips were then placed on top of the outer STAR® wire. A cartridge heater was used to heat the Cu rod. As indium started melting, we added more to fill the groove. Solder flux was sprayed into the groove at 100 °C and to the molten indium at about 160 °C before turning off the heater.

The entire fabrication process, including warmup and cooldown, took about 15 minutes. The temperature of the Cu rod and STAR® wires remained between 150 °C and 160 °C for about five minutes. We removed the excessive indium to maintain the cylindrical shape of the rod after the indium solidified (figure 4).

We inserted Layer 1 into Layer 2 to assemble the s0 magnet. Both layers were then aligned longitudinally and azimuthally via bronze rods through the alignment holes located near the mandrel ends. Three sets of Kapton shims, each 0.559 mm thick and 120° apart, were inserted into the radial clearance between the two layers to radially center both layers.

The wire terminations from both layers were joined electrically in a praying-hand configuration at the return end of the magnet. The terminations were sandwiched between two Cu blocks with indium foil covering the mating Cu surfaces. We then fastened the Cu blocks using screws to form a pressure contact between the Cu and indium foils.

Figure 5 shows the assembled s0 magnet. The magnet and inter-layer joint were attached to a G10 strongback. The STAR® wires at the lead end were bent and attached to a pair of vertical current leads from the test header. We determined the final positioning of the magnet and STAR® wires using a mock-up coil made of a cardboard tube and Cu refrigeration tubing.

At the magnet lead end, the wires of each layer were separated by a maximum distance of 11 mm to accommodate the current transducers and current-imbalance sensors that

will be described in section 3.1. To reduce the impact of electromagnetic forces on the separated wires, we secured the STAR® wires using five G10 spacers distributed along the arc of the bent wires. Each wire stayed inside a slot on the G10 spacer and was secured using waxed strings. Four printed wire separators were also used to support the wires (figure 7(b)).

3. Experimental setup and measurements

3.1. Instrumentation

The voltage across each layer of the magnet was measured using voltage taps embedded inside the electrical terminations. The voltage tap was about 5 mm away from the magnet-facing end of the termination. Figure 6 shows the electric circuit of the magnet during the tests and the locations of the voltage taps. The current flowed from Layer 1 to Layer 2.

Two types of sensors were used to measure the current distribution in the STAR® wires.

The first type is a current transducer similar to the one described in [54]. The objective of using the current transducer is to measure the current in a STAR® wire. The transducer consisted of a Hall sensor (F.W.Bell® FH-301-020) and two half yokes surrounding the STAR® wire. The yoke was made of low-carbon 1018 steel (figure 7(a)). The current in each STAR® wire was measured by a dedicated current transducer. Two current transducers were placed in a polyether-ether-ketone (PEEK) base for each magnet layer. A G10 spacer separated the transducers by 1 mm to reduce the crosstalk between the transducers. The Hall sensors were glued to the yoke using VGE-7031 varnish. Appendix A has more details on the calibration results.

The second type is a current-imbalance sensor that measures the magnetic field generated by the differential current between the two STAR® wires, following [55–57]. The sensor consisted of a Hall sensor (F.W.Bell® FH-301-020) placed in between, and coplanar with, the two STAR® wires via a printed spacer (figure 7(b)). Appendix B has more details on how we interpret the data from the current-imbalance sensor.

The dipole field in the magnet aperture was measured using a calibrated cryogenic Hall sensor (F.W.Bell® BHA-921).

The cryogen level was continuously monitored to ensure that the STAR® current leads and magnet were submerged in the cryogen during the test. We installed two calibrated Cernox® temperature sensors in the cryostat to monitor the test temperature: one at the maximum height of the STAR® wires at the magnet lead end and the other at the bottom of the cryostat.

We used two data acquisition (DAQ) systems.

The first system consisted of digital multimeters (Keithley 2010, 2182A, and 2700) and a temperature monitor (Lakeshore 218), all controlled by a laptop via a GPIB bus. In addition to the temperatures, the recorded data included the magnet current, voltages across each layer of the magnet and voltages across the current leads. The system also recorded the output from the Hall sensor measuring the dipole field and the output from the current transducers. The sampling rate was about 0.3 Hz.

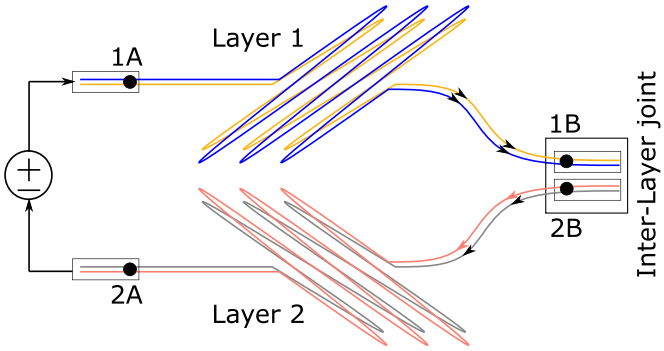

Figure 6. The circuit of s0 test and the locations of the voltage taps. The voltage across Layer 1 is given by Taps 1A and 1B; the voltage across Layer 2 is given by Taps 2B and 2A. The voltage across the inter-layer joint is given by Taps 1B and 2B.

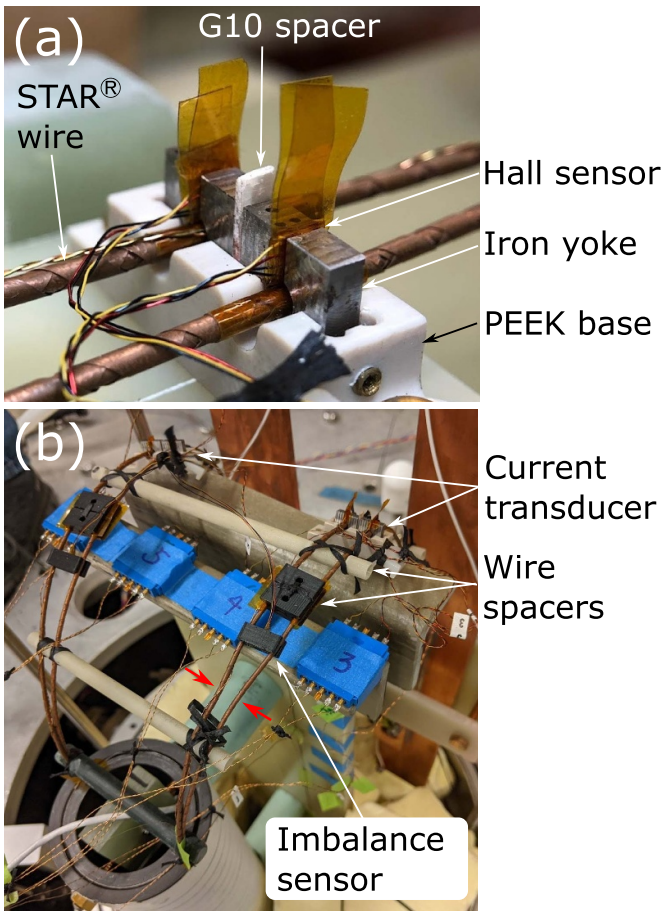

Figure 7. Two types of current sensors are used for each layer of the s0 magnet. (a) A current transducer that measures the current in each STAR® wire. (b) An imbalance sensor that measures the differential current between the two STAR® wires. The red arrows indicate where the wires deformed during the test.

The second system was a National Instruments CompactDAQ (NI cDAQ) system including NI-9238 and NI-9239 cards. The system simultaneously digitized the magnet current, voltages across each layer, and the signals from the current transducers and current-imbalance sensors. The sampling rate was 1.6 kHz.

The voltage across each magnet layer, filtered and amplified by Keithley 2182A multimeters, was used for quench detection. The detection system shut down the power supply once the input voltage was above certain thresholds. No external resistor was used to extract the energy stored in the magnet.

A single-mode fiber was co-wound with the STAR® wires in Layer 2 to develop a procedure of using distributed fiber-optic sensing for future magnets. A commercial Luna ODiSI system was used to measure the spectrum shift of the optical signal during the tests at 77 and 4.2 K. The measurement frequency was 10 Hz. The spatial resolution was 0.65 mm along the fiber.

3.2. Measurements and data reduction

We measured the critical current and dipole field of each layer at 77 K, self-field, in April 2021. Layer 2 was measured again at 77 K in September 2021 to test the current transducers and current-imbalance sensors. We tested the assembled s0 magnet at 77 and 4.2 K in November 2021.

It took about 30 minutes to cool down each layer from room temperature to 77 K. It took about 160 minutes to cool down the assembled magnet in a vertical cryostat from room temperature to 77 K. The magnet was cooled down to 4.2 K after the 77 K test, when the thermometers inside the cryostat read around 100 K.

At 77 K, we measured the layer voltage and current when the current was held constant at various levels. We also ramped the current continuously at different rates to study the ramp-rate dependence of the magnet performance.

The magnet current was ramped continuously at a certain rate during the 4.2 K tests. The continuous current ramping caused a higher inductive voltage component in the voltage acorss each layer. We applied a moving average with a window size of 200 data points to the layer voltage and magnet current data acquired by the cDAQ system. The averaged data are reported here.

4. Magnet test results at 77 K

4.1. Conductor critical current at 77 K

We determined the critical current, I_c, and n value by fitting the measured $V(I)$ data according to a power law [58]

$$V = V_o + IR_t + V_c\left(\frac{I}{I_c}\right)^n, \qquad (2)$$

where V_o is the voltage offset, R_t is the termination resistance, and V_c is the voltage criterion. Here we define I_c and n values using a V_c of 20 μV, corresponding to an electric-field criterion of about 10 μV m^{-1}.

Table 2 gives the I_c and n value of the five STAR® wires measured at 77 K, self-field, based on the data reported in [24]. Wires A and B were paired for Layer 1 and Wires D and E were paired for Layer 2. We used Wire C to develop the termination concept and calibrate the current transducers.

Table 2. I_c and n value of the five STAR® wires measured by AMPeers at 77 K, self field. The voltage criterion is 20 μV.

Wire #	I_c (A)	n	Used in s0 as
A	419	21.9	Layer 1 Wire 1
B	416	17.2	Layer 1 Wire 2
C	474	20.0	—
D	431	19.0	Layer 2 Wire 1
E	436	22.0	Layer 2 Wire 2

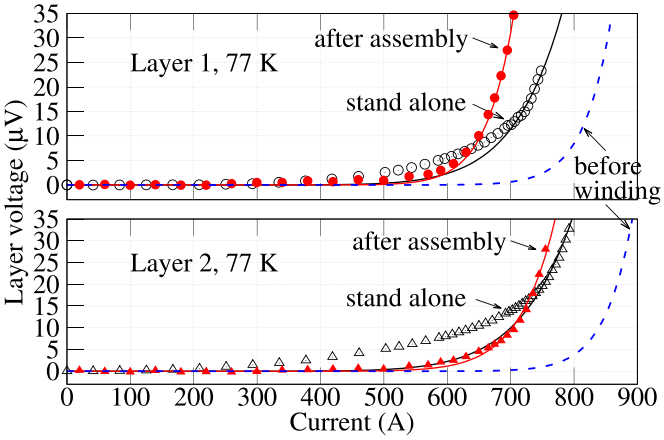

Figure 8. Measured voltage across each layer as a function of current at 77 K. Black open symbols: each layer tested stand-alone; red closed symbols: after assembly into s0. The solid lines are the exponential fit of the measured $V(I)$ data according to (2). The blue dashed lines are the calculated $V(I)$ curves for each pair of wires, before winding, based on the data from table 2.

4.2. Current-carrying capability of the magnet at 77 K

Figure 8 shows the $V(I)$ transition for each layer measured at 77 K, self-field. The I_c decreased by 12% in Layer 1 and by 14% in Layer 2 after winding, compared to the theoretical I_c before winding (table 3). After the magnet was assembled, the I_c further decreased by 8% in Layer 1 and by 2% in Layer 2. We observed an early voltage rise starting from around 300 A in Layer 1 and around 200 A in Layer 2, when each layer was tested individually. The early voltage rise was less pronounced after the magnet assembly (figure 8).

4.3. Current distribution between the STAR® wires at 77 K

Figure 9 shows the Layer 1 voltage, the output voltage of the current-imbalance sensor and the current ratio between the two wires, measured during Ramp 4 at 77 K. The slope of the imbalance voltage changed around 520 A when the layer voltage started rising.

4.4. Dipole transfer function at 77 K

Figure 10 shows the measured and calculated dipole-field transfer function at 77 K. The transfer function is defined as the ratio between the dipole field at the center of the magnet aperture and magnet current. The dipole field at the center of the coil aperture was measured during the test of each individual

Table 3. I_c and n value of each layer of the s0 magnet, determined at a voltage criterion of 20 μV according to (2). The I_c and n value for each pair of wires before winding were determined from the calculated $V(I)$ in figure 8. The I_c of Layer 2 at 4.2 K is extrapolated from the measurement data according to (2).

	77 K		77 K		77 K		4.2 K		4.2/77 K
	Before winding		After winding		After assembly		After assembly		I_c ratio
Layer	I_c (A)	n (–)	I_c (A)	n (–)	I_c (A)	n (–)	I_c (A)	n (–)	(–)
1	836	19.6	739	10.3	681	16.2	8723	21.3	12.8
2	868	20.5	752	9.7	739	13.6	9258	7.4	12.5

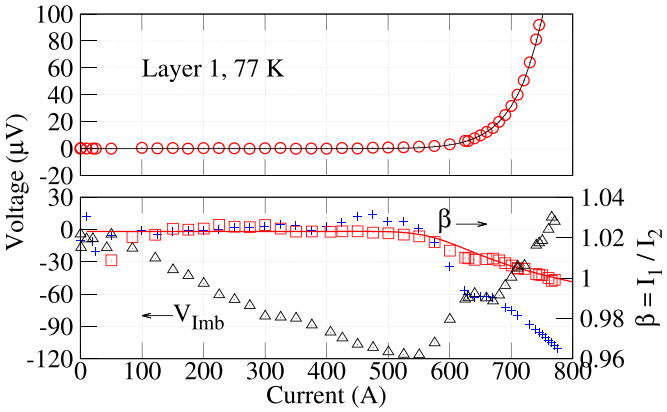

Figure 9. Top: Voltage across Layer 1 as a function of current. Bottom: The output voltage of the current-imbalance sensor, V_{imb}, on the primary y-axis and the current ratio, $\beta = I_1/I_2$, on the secondary y-axis. The output voltage of the current-imbalance sensor was shifted along the y-axis to start from zero at zero current. Two sets of current-ratio data are shown: the blue crosses are determined by the current measured by the current transducers and the red squares are determined using the method described in appendix B. The solid lines are the calculated $V(I)$ and current ratio described in appendix C.

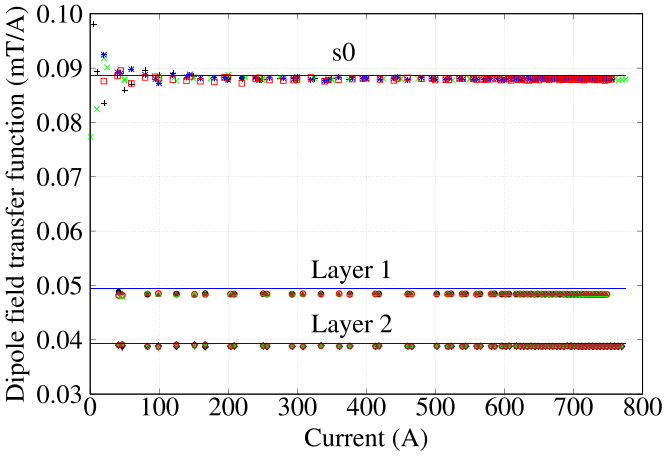

Figure 10. The dipole-field transfer function of individual layers and assembled magnet at 77 K. Lines: calculation. Symbols: measurements using direct current. The calculation assumed that both wires carried identical current in each layer.

layer. The measurements were performed using direct current (DC). Compared to the calculation, the measured dipole transfer function is about 2% lower for Layer 1, 1% lower for the Layer 2, and 0.6% lower for the assembled s0 magnet.

5. Magnet test results at 4.2 K

5.1. Magnet performance with respect to the short-sample prediction

Figure 11 shows the voltage across each layer during Ramp 14 when the magnet reached 8908 A, the highest current of all the ramps. The voltage across Layer 1 started rising around 6700 A. The voltage across Layer 2 started rising around 3800 A.

We determined the performance limit of the s0 magnet based on the $I_c(B)$ data for Wire 1 of Layer 1 because it is expected to experience the highest field among all four wires. The resulting performance limit is called the short-sample prediction (SSP).

Lacking the actual $I_c(B)$ data for Wire 1 of Layer 1 at 4.2 K, we used the data from STAR® #1 in [25] as an approximation, because both wires have the same number of tapes and nominal wire diameter. The $I_c(B)$ of STAR® #1 follows a scaling law of

$$I_c \propto B^{-0.818}, \tag{3}$$

where B is the applied magnetic flux density ranging from 18 to 31 T [25]. We used (3) to extrapolate the $I_c(B)$ data down to 2 T.

Figure 12 shows the magnet load lines, short-sample prediction, and measured dipole field for s0 at 4.2 K from Ramp 14.

The expected short-sample prediction for s0 is 11 382 A, assuming that both wires in each layer carry the same current. Layer 1 started transitioning at 59% of the SSP, and reached 78% of the SSP at a peak current of 8908 A. The current corresponds to a whole-conductor current density of 1500 A m^{-2}. We measured a peak dipole field of 0.79 T at the center of s0's aperture.

5.2. Degradation of critical current and burn-out in Layer 1

The $V(I)$ of Layer 2 was largely reproducible among all the current ramps at 4.2 K, despite the early rise of the voltage around 3.8 kA (figure 13).

The critical current of Layer 1, however, degraded after Ramp 14, as evidenced by the $V(I)$ curves shown in figure 14. Table 4 lists the I_c and n values of Layer 1 for each ramp. The $V(I)$ curves of the earlier ramps, whose peak currents were below 7.5 kA, followed that of Ramp 11 in figure 14.

Figure 15 shows the current ratio between the two wires and voltages of Layer 1 during Ramp 14 with a minimum I_c

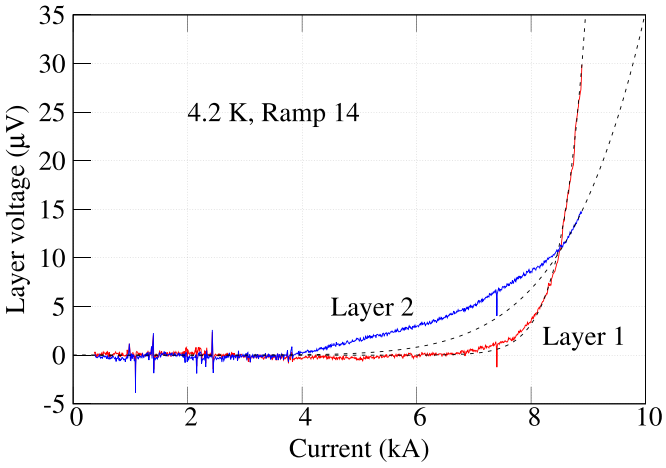

Figure 11. Voltage across each layer during Ramp 14 at 4.2 K. The dashed lines are exponential fit to the measurement when the current is above 8.5 kA. The ramp rate of the current was 30 A s^{-1} on average.

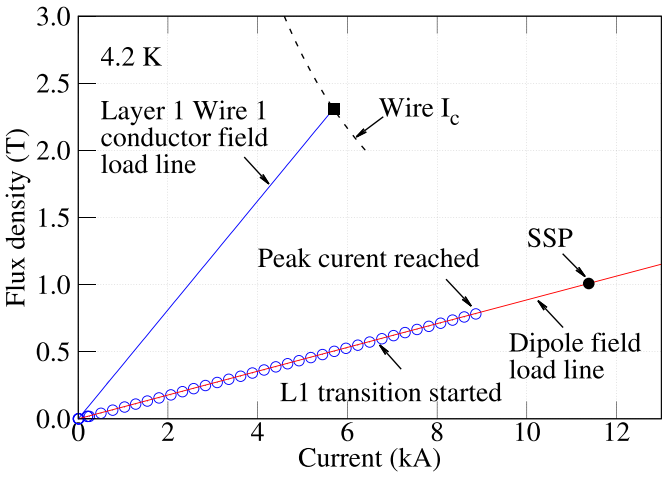

Figure 12. Expected performance limit for s0. The blue solid line is the conductor peak field load line. The dashed line shows the $I_c(B)$ data extrapolated from the data of STAR® #1 [25]. The solid black square point gives the expected limit: 5691 A in Layer 1 Wire 1 with a peak field of 2.31 T on the wire. Blue open circles represent the measured dipole field.

degradation and Ramp 20 with a maximum degradation. We plotted the data for 4 kA and above to highlight the change of the current ratio and layer voltage.

The voltage across Layer 1 voltage went above 0.6 V at 8895 A during Ramp 20, followed by an open circuit in Layer 1. We found that Layer 1 burned out locally after the magnet disassembly. Figure 16 shows that a 10 mm long section was damaged in both wires. Within the damaged section, about 3 mm long of wire was missing. The Cu instrumentation wire broke at the burned section. The outer tapes also appeared damaged in the wire of the neighboring turn, below the burned location.

The burned location was roughly −5 mm away from the mid-plane along the y direction, close to the expected −6 mm (figure 1). Along the z direction, the burned location was at about $z = -2$ mm, close to the expected $z = -2.2$ mm. The

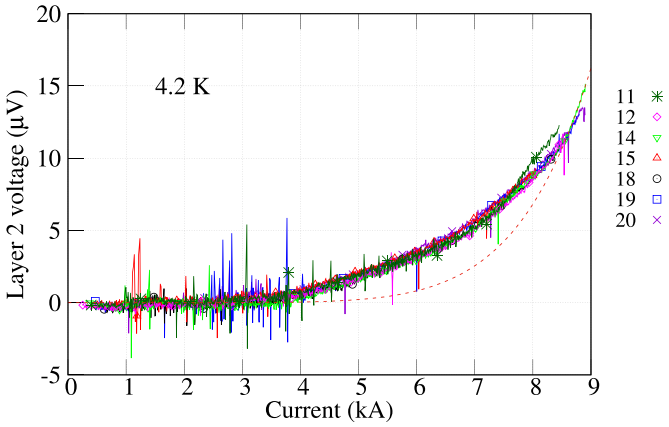

Figure 13. Layer 2 voltage as a function of magnet current. The ramp rate of the current was 30 A s^{-1} on average. The dashed line is the fit of the $V(I)$ data for the current above 8.5 kA according to (2). The ramp number and corresponding data legend are given on the right side of the figure.

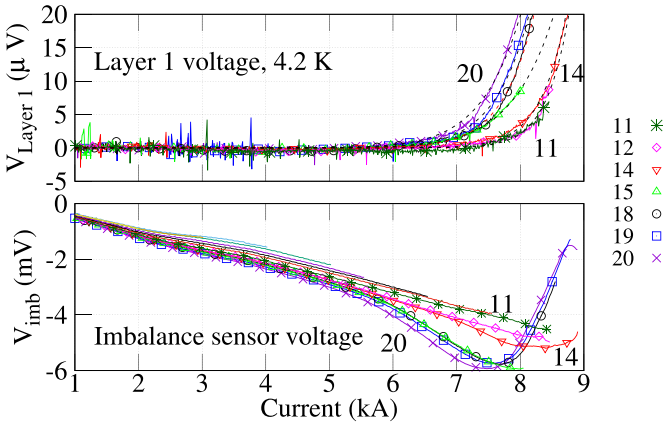

Figure 14. Top: Layer 1 voltage in μV as a function of magnet current. The dashed lines are the fit of the $V(I)$ data according to (2). Bottom: The output voltage of the current-imbalance sensor in mV. The bottom graph also includes the data from earlier ramps with a peak current ranging from 1 to 7.5 kA. The ramp rate of the current was 30 A s^{-1} on average. We labeled Ramps, 11, 14 and 20 next to the data.

Table 4. Degradation of the I_c and n value of Layer 1 at 4.2 K. I_c and n-value are determined at a 20 μV criterion according to (2). The changes in I_c, ΔI_c, and the changes in n values, Δn, are with respect to the values of Ramp 11.

Ramp	I_{max} (A)	V_{max} (μV)	I_c (A)	ΔI_c	n (–)	Δn
11	8493	7.6	8764	0.0%	24.5	0%
12	8570	10.2	8764	0.0%	24.5	0%
14	8908	30.7	8723	−0.5%	21.3	−13%
15	8056	10.3	8531	−2.7%	13.0	−47%
18	8554	35.5	8219	−6.2%	16.3	−33%
19	8844	72.4	8141	−7.1%	14.9	−39%
20	8895	burn-out	8006	−8.6%	13.1	−47%

longitudinal center of the mandrel is located at $z = 0$ mm. The center of the burned section in each wire shifted by 1–2 mm (figure 16(b)).

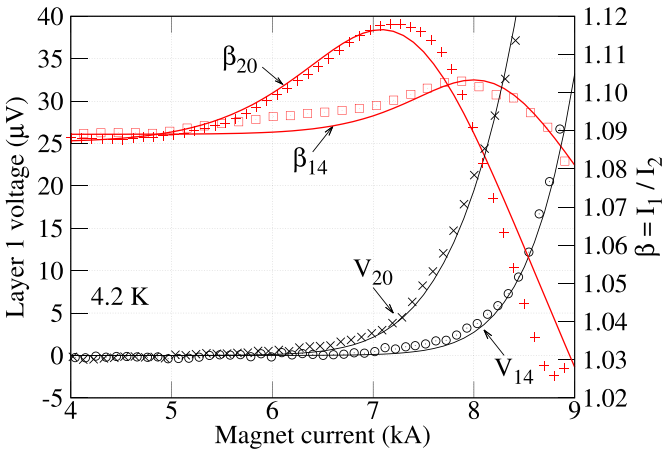

Figure 15. The measured voltage across Layer 1 and the current ratio between the two wires during Ramps 14 and 20 (symbols). The solid lines are the calculated results based on the method described in appendix C.

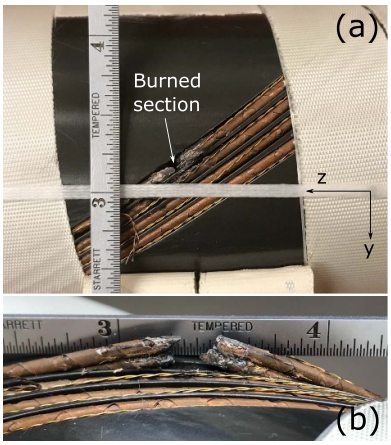

Figure 16. (a) The wires burned about 5 mm above the mid-plane as represented by the horizontal waxed string. (b) The ends of both wires fused together. The scale in the pictures is in inches.

5.3. Conductor deformation and displacement during magnet energization

The lead wires in both layers deformed due to the electromagnetic force at multiple locations where the wires were separated to accommodate the current sensors, especially at the sections that were not supported. The red arrows in figure 7(b) point to one such example.

The optic fiber along the STAR® wires in Layer 2 also indicated that the wires in the mandrel grooves might have moved due to the electromagnetic forces. Figure 17 shows the spectral shift and the corresponding strain data from the fiber at two locations along the winding, when Layer 2 was tested stand-alone at 77 K. At Location A, the mid-plane region of the magnet, the spectral shift indicated that the fiber and likely the STAR® wire were under tension. At Location B, near the pole region, the fiber and likely the wire were in compression.

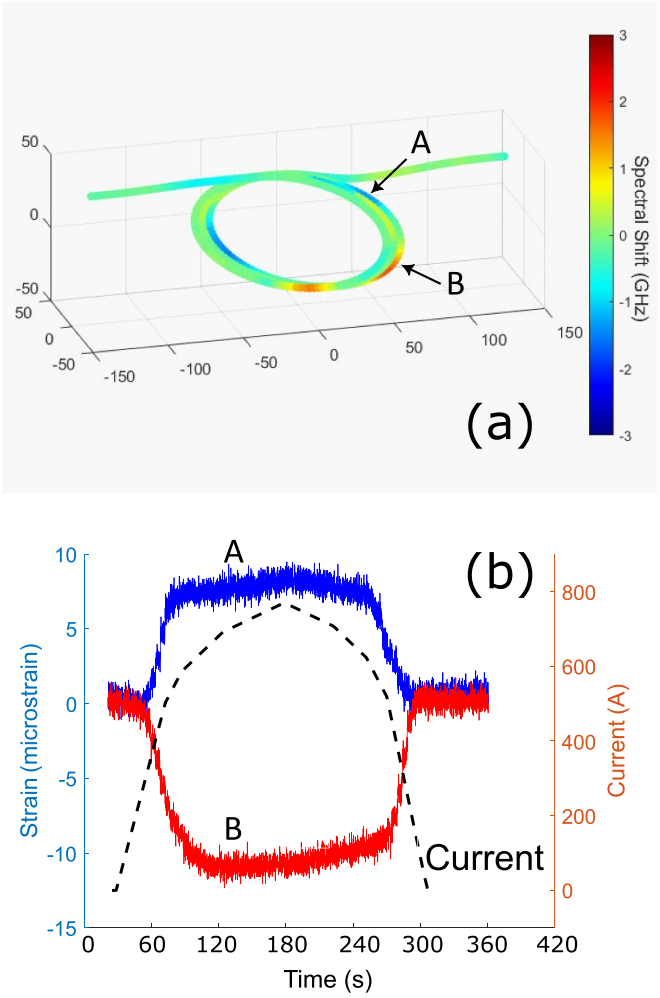

Figure 17. The spectral shift data from the fiber along the STAR® wire in Layer 2, 77 K. Positive shift means compression and negative shift means tension. (a) Spectral shift data along the coil at the peak current. (b) The strain data at Locations A and B during the current ramp. Location A is near the mid-plane region and Location B is near the pole region.

The amplitude of the spectral shift at 4.2 K was higher than at 77 K and saturated the instrument when the current was above 4 kA.

6. Ramp-rate dependence of the current distribution

Figure 18 shows the ratio of the current in the wires of Layer 1, as a function of current and its ramp rate at 77 K. The current ratio was determined using the method described in appendix B. The current ratio increased with the ramp rate. Both wires carried a similar current when the total current approached the layer I_c.

Figure 19 shows the ramp-rate dependence of the current ratio of Layer 1 at 4.2 K. The current ratio again increased with the ramp rate, but to a lesser degree than that seen at 77 K.

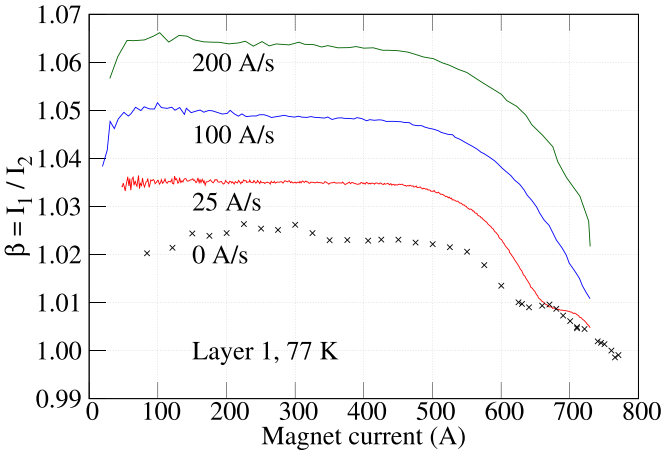

Figure 18. The ratio of the current in the wires of Layer 1 at different ramp rates, 77 K. The data for the DC case are from figure 9.

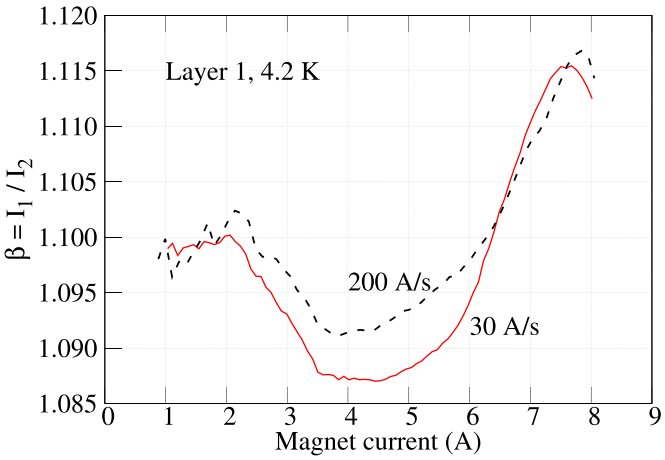

Figure 19. The ratio of the current in the wires of Layer 1 at different ramp rates, 4.2 K.

7. Electrical resistance of the terminations

Figure 20 shows the voltage across the praying-hand joint between the two layers as a function of current at 77 and 4.2 K. The voltage was reproducible during all current ramps. The joint resistance is 138 nΩ at 77 K and 21 nΩ at 4.2 K, based on the slope of the $V(I)$ curves in figure 20.

Table 5 gives the termination resistance of each layer, based on the measured $V(I)$ data at low current according to (2).

8. Discussion

8.1. Continue developing magnets using STAR® wires toward higher dipole fields

The s0 magnet provided an initial answer to the question of how to use STAR® wires to make dipole magnets. Leveraging the small wire diameter, we can use multiple STAR® wires to increase the magnet current. We wound two wires in each layer

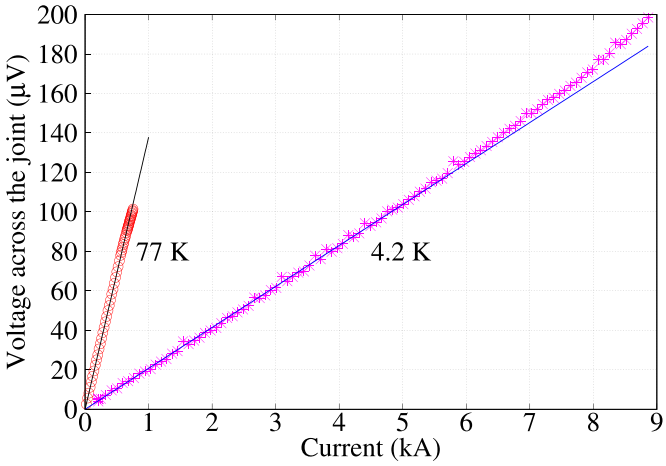

Figure 20. Voltage across the inter-layer joint, as a function of current, at 77 and 4.2 K, self-field. Symbols: measurement data; lines: linear fit of the data.

Table 5. Termination resistance in nΩ at 77 and 4.2 K.

Layer	77 K	4.2 K	Ratio
1	66	11	6.0
2	151	23	6.6

of s0. The wires, after the coil winding, formed a ribbon-type cable without transposition.

The transport performance of Layer 1 showed that the wires worked reasonably well. Layer 1, featuring the smallest bend radius and highest conductor fields, reached 78% of the short-sample prediction at 4.2 K. This can be a conservative estimate for two reasons. First, the reference wire, STAR® #1 in [25], can have a higher I_c at 4.2 K than that of the actual s0 wire. The 77 K I_c of the reference wire is 22% higher than that of Layer 1 Wire 1 before winding. The REBCO tapes in both the reference wire and the wires used in s0 were made by a similar process. The fabrication process and the resulting pinning characteristics in the REBCO tapes suggest that a higher I_c at self-field, 77 K, leads to a higher I_c in field, at 4.2 K. Second, the scaling law (3), determined at high fields, can overestimate the I_c at fields below 3 T as the conductor self-field becomes more pronounced.

The burnout at the expected peak-field location in Layer 1 provided a necessary condition that the magnet reached its intrinsic limit and the performance was not limited by potential conductor degradation at unexpected locations.

The s0 magnet also showed that we have a reasonable technique to make electrical terminations for a two-wire cable. The resistance across the praying-hand inter-layer joint at 4.2 K (figure 20) was comparable to those of CORC® wires in a recent magnet [49]. The reasonable joint resistance allowed us to probe the magnet performance, critical for further magnet development.

In addition, both wires of each layer had similar termination resistance. The measured current ratio at low current of the s0 magnet indicated that the termination resistances for

Table 6. The expected dipole field from CCT dipole magnets in various background dipole fields at 4.2 K. The dipole transfer function (TF) is also included. Each magnet has a 50 mm clear aperture and uses two STAR® wires. The dipole field reported here is the short-sample prediction based on the measured $I_c(B)$ data of STAR® #1 in [25]. The magnets do not have iron.

Layers	TF (T kA^{-1})	OD (mm)	0 T (T)	8 T (T)	12 T (T)	15 T (T)
2	0.34	77	2.9	1.2	0.9	0.8
4	0.71	105	4.5	2.4	1.9	1.6
6	1.10	135	5.8	3.4	2.7	2.4

the wires were within 5% in both layers, following the analysis in [59–61]. The similar and low termination resistance for each wire allowed current to redistribute between the two wires (figures 9 and 15), maximizing the current-carrying capability of the ribbon-type cable.

The s0 magnet, however, is not perfect in terms of the transport performance. The persistent and early voltage rise in Layer 2 at both 77 and 4.2 K suggested that some of the tapes may have degraded in the wires. The test of Layer 2 at 77 K (figure 8) indicated that the degradation may have already occurred, for instance, during wire handling and coil winding. In addition, the 88% I_c retention of Layer 1 at 77 K after winding (table 3) is lower than the 95% retention of a similar CCT coil wound with a single STAR® wire [24].

Although the s0 performance had significant room for improvement, the initial experiment generated a minimum set of viable tools to further develop the magnet technology. We need to continue developing magnets to gain data and experience on using STAR® wires to generate higher dipole fields.

Given the minimum set of tools and a longer two-wire ribbon-type cable configuration, what field can we expect for a CCT dipole magnet? table 6 lists the performance of a few CCT dipole magnets having an increasing number of layers. The radial thickness of each layer in these conceptual designs is identical to those in the s0 magnet. Each magnet has more conductor turns than s0 to generate a uniform dipole field along the magnet center region.

The conceptual CCT dipole magnet designs in table 6 promise a higher dipole transfer function and a smaller outer diameter, compared to the existing CORC® CCT magnets [48, 49]. The STAR®-based CCT dipole magnets can therefore be well suited for operation inside the limited aperture of Nb_3Sn dipole magnets [42, 62].

The current-imbalance sensor reported here is one example of the magnetic quench-detection approach [63]. Our experiment, together with the earlier ones [56, 57], suggested that the technique can be highly sensitive to the current redistribution that is associated with voltage buildup, allowing prescient warning of conductor heating. Testing longer magnets is necessary to verify if the technique is equally effective for longer conductors.

One tool that is missing for further magnet development is an impregnation technique. Although the STAR® wires can be resilient to the mechanical deformation and the resulting strain during the test (figures 7 and 17), we should avoid conductor deformation during magnet operation. Built on the significant experience that the community has gained [10, 64–72], a vacuum-pressure impregnation technique should be developed to support individual REBCO tapes in a STAR® wire.

The experiment with the optic fiber demonstrated that the fiber can operate at 4.2 K. A successful impregnation technique will benefit future tests of the optic fiber toward identifying the hot spots along REBCO cables [73] and ultimately the detection of normal transitions [74, 75].

8.2. Continue developing STAR® conductors based on the feedback from magnet results

The development of the s0 magnet confirmed the wire flexibility that was demonstrated on short STAR® wire samples. Wire 1 of Layer 1 has a minimum bend radius of 15.4 mm at six locations along the pole regions of the s0 magnet (figure 1). The transport performance of Layer 1 at 77 and 4.2 K suggested that the 15 mm minimum bend radius can be reproduced in a 2 m long wire at multiple locations, consistent with the experience of an earlier STAR®-based CCT coil of a similar design [24].

It is necessary to demonstrate a uniform wire diameter and critical current over a length of the order of 10 m or longer as a next step for future magnet experiments. [24] reports a 10 m long STAR® wire. The wire diameter varies within $\pm 2\%$ of the mean diameter, likely sufficient for further magnet practice. The critical current, measured every 1 m along the wire, varies more.

The degradation of current-carrying capability is a serious issue that should be avoided for applications. The current-carrying capability of Layer 1 clearly degraded after Ramp 14 that reached a peak current of 8908 A (figure 14 and table 4), and continued degrading in the following ramps. Based on the measured $V(I)$ transition of Layer 1 and the current ratio β, we conclude that both wires degraded, consistent with the observed burn-out. The critical current and n value decreased in both wires, leading to the change in β during various current ramps (figure 15). Appendix C has more details on the analysis.

We suspect that the conductor heating during the superconducting-to-normal transition caused the degradation in Layer 1. We assumed that a 5–7.5 mm long section in both wires, consistent with the burn-out, absorbed an equal amount of heat under an adiabatic condition. The estimated peak temperature during Ramps 11–19 ranged from 440 to 1040 K, high enough to degrade the critical current of REBCO tapes [76, 77]. A recent CORC® dipole magnet suffered a similar critical-current degradation, possibly also due to the conductor heating [49].

Although Layer 2 consistently showed an early voltage rise, the critical current of Layer 2 remained the same among various current ramps (figure 13). We attribute the degradation-free behavior to the effective cooling from the surrounding cryogen. A similar behavior was also observed in the outermost layer in the CORC® dipole magnet [49].

We can avoid excessive heating in the first place if a sufficient current margin exists between the operating and

current-sharing levels. A higher critical current in REBCO cable is necessary to enable this margin.

When a sufficient margin yields to the desire of a higher magnet efficiency, the ever higher current-carrying capability exacerbates the situation: more heating in a shorter time. Therefore, we also need sensitive schemes to detect soon enough the early temperature rise in a magnet.

Lacroix *et al* has demonstrated a concept of current flow diverter that significantly boosts the propagation of normal zones in REBCO tapes [78]. Since a fast propagation of the normal zone can improve the sensitivity of the voltage-based quench detection, it can be useful to test the concept using STAR® wires and verify its impact on quench detection.

A larger fraction of low-resistivity Cu stabilizers in STAR® wires can also help reduce the peak conductor temperature. For instance, a 1.024 mm diameter Cu former will increase the Cu to non-Cu ratio from 0.51 to 0.80 in the STAR® wire used in the s0 magnet. The resulting peak temperature can decrease by about 20% for the same amount of heat over a 5 mm long wire section.

We also need a higher current-carrying capability in STAR® wires to reach higher fields, in addition to a sufficient operating margin. The critical current should at least double or triple for the reference STAR® #1 in [25] at 20 T, 4.2 K in order for the four- and six-layer conceptual insert magnets to generate a dipole field of 5 T in a background field of 15 T (table 6)[4]. Alternatively, we need a cable containing multiple STAR® wires to increase the magnet transport current, while maintaining a small bend radius similar to that of a single wire.

Multiple STAR® wires can be connected electrically in series or parallel to achieve the same ampere-turns in a magnet. For s0, we chose the latter for two reasons. First, it mitigates the potential risk of local I_c dropouts in the wires that can limit the magnet current if the wires are electrically in series. Second, the parallel configuration reduces the number of joints between the layers in the s0 magnet [38].

The parallel configuration, however, does not guarantee an even current distribution between the two wires (figures 18 and 19).

An uneven current distribution can affect the magnetic field quality. Using the two-layer CCT dipole magnet described in table 6 as an example, we expect the uneven current distribution to affect mainly the dipole field but not the high-order geometric multipoles (appendix D). The impact on the dipole field of individual magnets can lead to undesired random field errors for a group of magnets in a collider. To clarify these effects, we need to measure and confirm the actual impact on field quality.

[4] The critical current of REBCO round wires decreases as the applied magnetic field, transverse to the longitudinal axis of the wire, increases. If the increased I_c at 20 T leads to a similar gain in I_c at low fields, then the insert magnet, when tested stand-alone, will generate a dipole field ranging from 10 to 15 T, or higher (table 6). The high stand-alone dipole field, consistent with the findings in [62, 79], explains the need to achieve higher fields in REBCO dipole magnets.

The ramp-rate dependence of the current distribution can be an intrinsic feature of the non-transposed multi-wire cable configuration. If further magnet experiments necessitate a uniform current distribution among the wires, we need to develop a transposed cable architecture using STAR® wires [80].

9. Conclusions

We made s0, a two-layer three-turn CCT dipole magnet, as an initial experiment on the magnet development using high-temperature superconducting STAR® wires. We developed a minimum set of tools for the magnet development. We wound in each layer two STAR® wires, one at a time, using a semi-automated winding table. The wires, electrically in parallel, formed a non-transposed ribbon-type cable. The minimum bend radius was 15.4 mm along the longitudinal axis of the STAR® wire. The electrical resistance of the terminations ranged from 11 to 23 nΩ at 4.2 K. The termination resistances for both wires were also uniform within 5%. The magnet reached a peak current of 8908 A at 4.2 K, 78% of the short-sample prediction, and a peak dipole field of 0.79 T. The peak current corresponded to a whole-conductor current density of 1500 A mm^{-2}.

The test results also highlighted several critical issues to be addressed: the critical-current degradation during current ramps; the necessity of a transposed multi-wire cable architecture for high-field dipole magnets; and an impregnation technique for STAR® wires.

The initial experiment of the s0 magnet set a stage for future development of STAR® magnets and conductors. The continued development can ultimately lead to diverse options of REBCO technologies to enable high-field magnets for particle accelerators and fusion machines.

Data availability statement

All data that support the findings of this study are included within the article (and any supplementary files).

Acknowledgments

J K, S K, J S S and V S developed the STAR® wires and measured their critical current at 77 K before winding. R L and W B G designed the magnet mandrels. W B G, with input from H C H, developed Winding table Mark #2. H C H and W B G wound both layers. H C H developed the termination concept and technique for STAR® wires and instrumented both layers. H C H and T J B assembled the magnet and prepared for the magnet test. M A M designed and machined the current transducer assembly. R T developed the current-imbalance sensor and analyzed the data. L L implemented the optic fiber and analyzed the data. H C H, T J B, L L, R M, C S M, R T, M T and X R W tested the magnet.

We thank Makato Takayasu of the Plasma Science and Fusion Center, Massachusetts Institute of Technology for his discussion and guidance on the design and development of the

current transducers. We also thank Tengming Shen of LBNL for providing a power supply to test the assembled magnet at 77 K and Lucas Brouwer for providing VGE varnish.

The work at AMPeers LLC and University of Houston was supported by SBIR award DE-SC0015983 from the US Department of Energy, Office of High Energy Physics. The work at LBNL was supported by the U.S. Department of Energy, Office of Science, Office of High Energy Physics, through the US Magnet Development Program under Contract No. DEAC02-05CH11231. The work on the optic fiber was supported by the U.S. Department of Energy, Office of Science, Office of Fusion Energy Sciences under Contract No. DEAC02-05CH11231.

One of the authors (VS) has financial interest in AMPeers.

Appendix A. Calibration of current transducer

We calibrated all four current transducers using Wire C, at 77 K, in a dc condition. The current monotonically increased from zero to the maximum value in a stair-step fashion; the voltage reading of each transducer, measured using a Keithley 2010 multimeter, was recorded when the current was constant at each step. The measurement was repeated three times and the averaged voltage was used as the calibration data. The calibration data were linearly interpolated to determine the current in the STAR® wire.

One option to characterize the measurement error of the current transducer is to compare the sum of the measured current in each wire and the measured total current. Figure A1 shows that the error of the current transducer was less than 5% of the measured total current, up to 800 A, the maximum current for the calibration. The increasing error is due to the saturation of the low-carbon steel (figure 7).

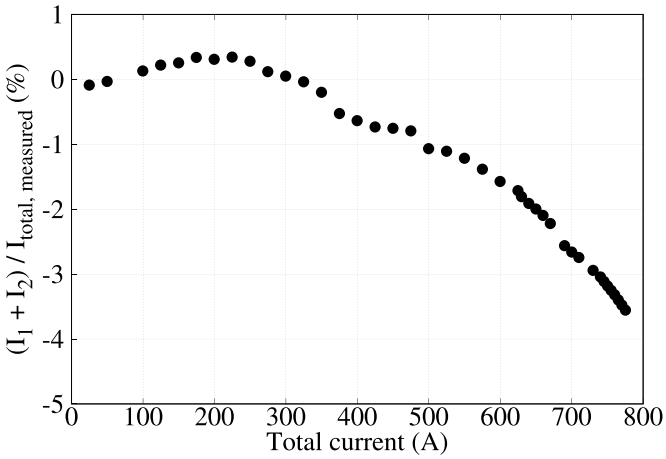

Figure A1. The relative difference between the sum of the wire current in Layer 1 and the measured total current, 77 K. The current in each wire, I_1 and I_2, is determined by the current transducer. $I_{total,measured}$ is the power supply output current measured by a shunt resistor.

Appendix B. Estimation of the wire current using the current-imbalance sensor data

Here we describe a method to determine the ratio of the current in the wires, based on the current-imbalance sensor data. Suppose we have two parallel line currents, I_1 and I_2, which have the same current direction and are separated by a distance of 2 r. The ratio of the current in the wires is β, and $\beta = I_1/I_2$. The total current carried by both wires, I_t, is then given by

$$I_t = (1+\beta)I_2. \tag{B.1}$$

The active sensing area of the Hall sensor is coplanar with both line currents and has an equal distance, r, to the line currents. The output voltage of the current-imbalance sensor is given by

$$V_{imb} = \omega(I_2 - I_1) = \omega I_t \frac{1-\beta}{1+\beta}. \tag{B.2}$$

Here ω is a constant and is given by

$$\omega = s\frac{\mu_0}{2\,\pi r}, \tag{B.3}$$

where s is the sensitivity of the Hall sensor in V T^{-1} and μ_0 is the magnetic permeability in vacuum.

Equation (B.2) shows that the output voltage of the current-imbalance sensor, V_{imb}, depends on the current ratio, β. When both wires carry the same current, $\beta = 1$ and $V_{imb} = 0$. When β is a non-unit constant, V_{imb} scales linearly with I_t. When the current redistributes between the two wires, β changes and V_{imb} deviates from the linear relationship with I_t. The sign of V_{imb} tells which of the two wires carries more current.

In the experiments reported here, I_t and V_{imb} are known. The current ratio is also known at low current from the current transducers. We can then determine ω according to equation (B.2), and then use the known ω to determine β for the current beyond the measurement range of the current transducers.

Appendix C. Estimation of the wire performance using the current ratio and measured cable *V*(*I*) data

Simple electric-circuit models are a powerful tool to explain the measured $V(I)$ behavior of REBCO tapes and cables [59–61, 81–83]. Here we use an approximate method, based on a dc electric-circuit model (figure C2), to interpret and gain insight on the performance of both wires in Layer 1 (table 4). We used NGSPICE [84], an open-source SPICE simulator, to analyze the circuit behavior.

Given that the wires have similarly low termination resistances and comparable critical currents, the electrical-parallel configuration of the wires implies that, using the same voltage criterion, the layer reaches its critical current when both wires also reach theirs too. Therefore, we have

$$I_{c,cable} \approx I_{c,1} + I_{c,2}. \tag{C.1}$$

In addition, when the layer voltage reaches the voltage criterion, we have

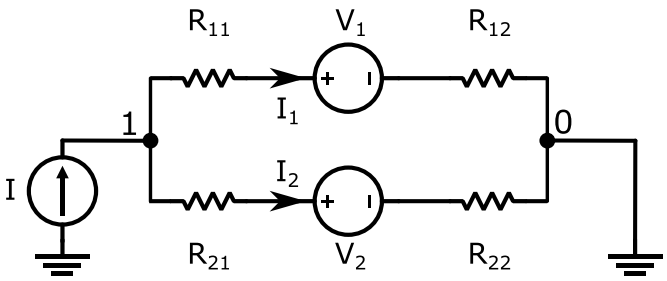

Figure C2. A dc electric-circuit model for two parallel STAR® wires in Layer 1 of the s0 magnet. V_n represents the measured voltage across Wire n, as a function of current, I_n. The termination resistance for Wire n, R_n, is given by $R_n = R_{n1} + R_{n2}$. The voltage across Nodes 0 and 1 represents the voltage measured across Layer 1 during the experiments.

Table C1. The measured critical current (A) and n value for Layer 1 and calculated values for individual wires at 77 and 4.2 K.

Ramp	$I_{c,cable}$	n_{cable}	$\beta(20\,\mu V)$	$I_{c,1}$	n_1	$I_{c,2}$	n_2
77 K, 4	680	16.5	1.01	341	16.9	339	16.0
4.2 K, 14	8764	21.3	1.09	4569	23.0	4195	16.5
18	8219	16.3	1.09	4281	23.0	3938	12.0
19	8141	14.9	1.09	4241	20.0	3900	11.5
20	8006	13.1	1.09	4174	18.0	3832	10.5

$$\beta(V = V_c) = \frac{I_{c,1}}{I_{c,2}}. \tag{C.2}$$

Using (C.1) and (C.2), we can determine the critical current of both wires.

After calculating the critical current of both wires, we estimate the n values by fitting the calculated $V(I)$ data to the measurement results. We assume the n value of the layer is between those of both wires. One may start the search with $n_{cable} \sim (n_1 + n_2)/2$.

The estimated critical current and n value of each individual wire qualitatively reproduce the measured layer voltage and current ratio. Figure 9 gives an example at 77 K. Figure 15 gives two more examples at 4.2 K. Table C1 gives the measured layer performance and calculated wire performance for the cases at 77 and 4.2 K.

Appendix D. Impact of current distribution on field quality

We consider only the dc geometric field errors due to transport current, assuming the as-designed conductor positioning [85]. Using the two-layer CCT dipole magnet described in table 6 as an example, we first define the transfer function for an individual wire. For instance, Wire 1 of Layer 1, carrying a current of I_1, has a transfer function

$$T_{n,L_1,W_1} = \frac{B_{n,L_1,W_1}}{I_1}, \tag{D.1}$$

where B_n is the magnetic field component of order n, generated by the current in Wire 1. We can calculate B_n using the Biot-Savart law. T_n has a unit of T A^{-1}.

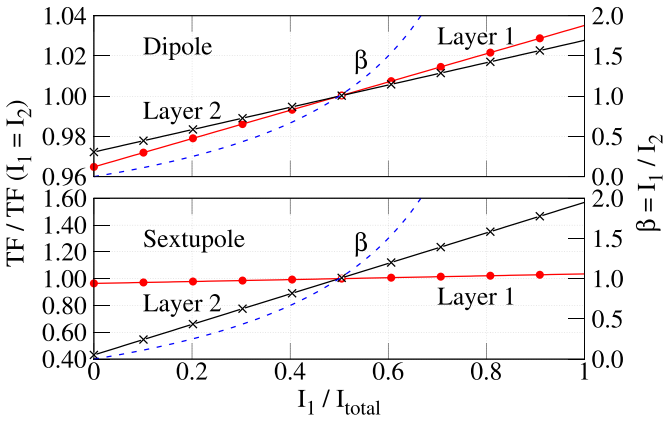

Figure D3. The transfer function of the dipole component (top) and sextupole component (bottom) for each layer, as a function of current distribution between the two wires, for the two-layer magnet design given in table 6. We normalize the transfer function to the value when both wires carry the same current. The red line with circles is for Layer 1. The black line with crosses is for Layer 2. The blue dashed line corresponds to the current ratio.

We define the transfer function of each layer as the following, again using Layer 1 as an example,

$$T_{n,L_1}(\beta) = \frac{T_{n,L_1,W_1} I_1 + T_{n,L_1,W_2} I_2}{I_1 + I_2}, \tag{D.2}$$

where the transfer function of each individual wire is given in (D.1). T_{n,L_1} depends on β, the current ratio between the two wires.

Figure D3 shows the impact of current distribution between the two wires on the dipole and sextupole field in the magnet aperture. When one wire carries all the current in both layers, the dipole transfer function is within 8% of the value where both wires carry the same current.

A 10% difference in the current of the two wires, as observed in the s0 magnet, leads to 0.4% of deviation from the case of an even current distribution. Therefore, the uneven current distribution cannot solely explain the observed discrepancy between the measured and calculated TF of each layer, tested stand-alone (figure 10). The positioning error of the Hall sensor can contribute to the discrepancy.

We expect the impact on high-order field errors to be negligible. Figure D3 shows the transfer function for the sextupole field, the first allowed high-order field errors in the example magnet here. Although the transfer function of Layer 2 can change by 60% when one wire carries all the current, it is not expected to be an issue because the sextupole field is four orders of magnitude lower than the main dipole field when $\beta = 1$.

ORCID iDs

Xiaorong Wang https://orcid.org/0000-0001-7065-8615
Timothy J Bogdanof https://orcid.org/0000-0003-2698-9016
Paolo Ferracin https://orcid.org/0000-0003-0415-8895
William B Ghiorso https://orcid.org/0000-0003-1083-4546
Stephen A Gourlay https://orcid.org/0000-0002-3813-5037
Hugh C Higley https://orcid.org/0000-0002-7137-3344
Janakiram Kaushal Kadiyala https://orcid.org/0000-0001-8930-549X
Soumen Kar https://orcid.org/0000-0001-5550-6859
Reginald Lee https://orcid.org/0000-0002-0333-6752
Linqing Luo https://orcid.org/0000-0002-7073-6588
Robert Memmo https://orcid.org/0000-0002-6493-9645
Cory S Myers https://orcid.org/0000-0002-7890-1883
Soren O Prestemon https://orcid.org/0000-0002-1937-4040
Jithin Sai Sandra https://orcid.org/0000-0003-2667-3716
Venkat Selvamanickam https://orcid.org/0000-0001-6618-9406
Reed Teyber https://orcid.org/0000-0001-6924-4175
Marcos Turqueti https://orcid.org/0000-0002-3892-1353
Yuxin Wu https://orcid.org/0000-0002-6953-0179

References

[1] D Schoerling and A V Zlobin (eds) 2019 *Nb_3Sn Accelerator Magnets* (Cham: Springer) (https://doi.org/10.1007/978-3-030-16118-7)
[2] Rossi L *et al* 2015 *IEEE Trans. Appl. Supercond.* **25** 4001007
[3] Rossi L *et al* 2018 *IEEE Trans. Appl. Supercond.* **28** 4001810
[4] Borgnolutti F, Durante M, Debray F, Rifflet J M, Rijk G D, Tixador P and Tudela J M 2016 *IEEE Trans. Appl. Supercond.* **26** 4602605
[5] Durante M, Borgnolutti F, Bouziat D, Fazilleau P, Gheller J-M, Molinié F and Antoni P D 2018 *IEEE Trans. Appl. Supercond.* **28** 4203805
[6] Rossi L and Senatore C 2021 *Instruments* **5** 8 and references therein
[7] Kirby G *et al* 2015 *IEEE Trans. Appl. Supercond.* **25** 4000805
[8] van Nugteren J *et al* 2018 *Supercond. Sci. Technol.* **31** 065002
[9] Uglietti D 2019 *Supercond. Sci. Technol.* **32** 053001 and references therein
[10] Hartwig Z S *et al* 2020 *Supercond. Sci. Technol.* **33** 11LT01
[11] van der Laan D C 2009 *Supercond. Sci. Technol.* **22** 065013
[12] Weiss J D, Mulder T, ten Kate H J and van der Laan D C 2017 *Supercond. Sci. Technol.* **30** 014002 and references therein
[13] van der Laan D C, Weiss J D and McRae D M 2019 *Supercond. Sci. Technol.* **32** 033001 and references therein
[14] Weiss J D, van der Laan D C, Hazelton D, Knoll A, Carota G, Abraimov D, Francis A, Small M A, Bradford G and Jaroszynski J 2020 *Supercond. Sci. Technol.* **33** 044001
[15] Gourlay S A, Prestemon S O, Zlobin A V, Cooley L and Larbalestier D 2016 (available at: https://escholarship.org/uc/item/5178744r)
[16] Prestemon S, Amm K, Cooley L, Gourlay S, Larbalestier D, Velev G and Zlobin A 2020 (arXiv:2011.09539)
[17] Gupta R 2019 (available at: www.bnl.gov/magnets/staff/gupta/publications/mt26/wed-af-or13-02-submit-2019-12-16.pdf)
[18] Kashikhin V, Lombardo V and Velev G 2019 Magnet Design Optimization for Future Hadron Colliders *The 10th Int. Particle Accelerator Conf. (IPAC2019)* (*Melbourne, Australia, 19–24 May 2019*) pp 4307–10
[19] Wang X, Caspi S, Dietderich D R, Ghiorso W B, Gourlay S A, Higley H C, Lin A, Prestemon S O, van der Laan D and Weiss J D 2018 *Supercond. Sci. Technol.* **31** 045007
[20] Luo W, Kar S, Xu A, Li X, Yahia A B and Selvamanickam V 2017 *IEEE Trans. Appl. Supercond.* **27** 6602705
[21] Kar S, Luo W, Ben Yahia A, Li X, Majkic G and Selvamanickam V 2018 *Supercond. Sci. Technol.* **31** 04LT01
[22] Luo W, Kar S, Li X, Galstyan E, Kochat M, Sandra J S, Jaroszynski J, Abraimov D and Selvamanickam V 2018 *Supercond. Sci. Technol.* **31** 12LT01
[23] Ben Yahia A, Kar S, Majkic G and Selvamanickam V 2019 *IEEE Trans. Appl. Supercond.* **29** 8401605
[24] Kar S, Sandra J S, Luo W, Yerraguravagari V, Galstyan E, Jaroszynski J, Abraimov D, Majkic G and Selvamanickam V 2020 *Supercond. Sci. Technol.* **33** 094001
[25] Kar S, Sandra J S, Luo W, Kochat M, Jaroszynski J, Abraimov D, Majkic G and Selvamanickam V 2019 *Supercond. Sci. Technol.* **32** 10LT01
[26] Meyer D and Flasck R 1970 *Nucl. Instrum. Methods* **80** 339–41
[27] Devred A 2003 High field accelerator magnets beyond LHC *Proc. Part. Accel. Conf.* (https://doi.org/10.1109/PAC.2003.1288864)
[28] Meinke R B, Ball M J and Goodzeit C L 2003 Superconducting Double-Helix accelerator magnets *Particle Accelerator Conf.* (*Portland, Oregon 12 –16 May 2003*) pp 1996–8
[29] Goodzeit C L, Ball M J and Meinke R B 2003 *IEEE Trans. Appl. Supercond.* **13** 1365–8
[30] Gavrilin A V, Bird M D, Bole S T and Eyssa Y M 2002 *IEEE Trans. Appl. Supercond.* **12** 465–9
[31] Akhmeteli A M, Gavrilin A V and Marshall W S 2005 *IEEE Trans. Appl. Supercond.* **15** 1439–43
[32] Akhmeteli A M, Gavrilin A V and Marshall W S 2006 *Superconductivity, Magnetism and Magnets* (Hauppauge, NY: Nova Publishers) ch 5 and references therein
[33] Caspi S, Trillaud F, Godeke A, Dietderich D R, Ferracin P, Sabbi G, Giloux C, Perez J G and Karppinen M 2009 *IEEE Trans. Appl. Supercond.* **19** 1195–8
[34] Bosi F, Paoloni E, Fabbricatore P, Farinon S, Musenich R, Marabotto R and Nardelli D 2012 *IEEE Trans. Appl. Supercond.* **22** 4000104

[35] Witte H, Yokoi T, Sheehy S L, Peach K, Pattalwar S, Jones T, Strachan J and Bliss N 2012 *IEEE Trans. Appl. Supercond.* **22** 4100110
[36] Caspi S *et al* 2014 *IEEE Trans. Appl. Supercond.* **24** 4001804 and references therein
[37] Brouwer L N 2015 *Canted-Cosine-Theta Superconducting Accelerator Magnets for High Energy Physics and Ion Beam Cancer Therapy Ph.D. Thesis* University of California, Berkeley (available at: https://escholarship.org/uc/item/8jp4g75g)
[38] Kirby G A *et al* 2018 *IEEE Trans. Appl. Supercond.* **28** 4002205
[39] Auchmann B, Brouwer L, Caspi S, Gao J, Montenero G, Negrazus M, Rolando G and Sanfilippo S 2018 *IEEE Trans. Appl. Supercond.* **28** 4000705
[40] Wu W, Liang Y, Zhou L-C, Mei E-M, Ni D-S, Zhen S-J, Ou X-J and Yang W-J 2020 *J. Phys.: Conf. Ser.* **1401** 012015
[41] Arbelaez D *et al* 2022 *IEEE Trans. Appl. Supercond.* **32** 4003207
[42] Brouwer L, Juchno M, Arbelaez D, Ferracin P and Vallone G 2022 *IEEE Trans. Appl. Supercond.* **32** 4001805
[43] Rudeiros Fernandez J L *et al* 2022 *IEEE Trans. Appl. Supercond.* **32** 4006505
[44] Godeke A *et al* 2015 *IEEE Trans. Appl. Supercond.* **25** 4002404
[45] Garcia Fajardo L, Brouwer L, Caspi S, Hafalia A, Hernikl C, Prestemon S, Shen T, Bosque E and English C 2019 *IEEE Trans. Appl. Supercond.* **29** 4002005
[46] Shen T and Garcia Fajardo L 2020 *Instruments* **4** 17
[47] Garcia Fajardo L *et al* 2021 *Supercond. Sci. Technol.* **34** 024001
[48] Wang X, Dietderich D R, DiMarco J, Ghiorso W B, Gourlay S A, Higley H C, Lin A, Prestemon S O, van der Laan D and Weiss J D 2019 *Supercond. Sci. Technol.* **32** 075002
[49] Wang X *et al* 2020 *Supercond. Sci. Technol.* **34** 015012
[50] Caspi S *et al* 2015 *IEEE Trans. Appl. Supercond.* **25** 4002304
[51] Brouwer L *et al* 2020 *Nucl. Instrum. Methods Phys. Res.* A **957** 163414
[52] Caspi S 2018 A video from Glyn Kirby on an automated winding table developed at CERN for a CCT Magnet
[53] Mulder T, Dudarev A, van der Laan D C, Mentink M G T, Dhallé M and ten Kate H H J 2015 Optimized and practical electrical joints for CORC type HTS cables *IOP Conf. Ser.: Mater. Sci. Eng.* **102** 012026
[54] Takayasu M, Chiesa L, Bromberg L and Minervini J V 2012 *Supercond. Sci. Technol.* **25** 014011
[55] Marchevsky M, Xie Y-Y and Selvamanickam V 2010 *Supercond. Sci. Technol.* **23** 034016
[56] Weiss J D, Teyber R, Marchevsky M and van der Laan D C 2020 *Supercond. Sci. Technol.* **33** 105011
[57] Teyber R, Marchevsky M, Prestemon S, Weiss J and van der Laan D 2020 *Supercond. Sci. Technol.* **33** 095009
[58] Iwasa Y 2009 *Case Studies in Superconducting Magnets: Design and Operational Issues* 2nd edn (Berlin: Springer) ch 6, p 370
[59] Zermeno V, Krüger P, Takayasu M and Grilli F 2014 *Supercond. Sci. Technol.* **27** 124013
[60] Willering G P, van der Laan D C, Weijers H W, Noyes P D, Miller G E and Viouchkov Y 2015 *Supercond. Sci. Technol.* **28** 035001
[61] Takayasu M, Chiesa L, Allen N C and Minervini J V 2016 *IEEE Trans. Appl. Supercond.* **26** 6400210
[62] Ferracin P *et al* 2022 *IEEE Trans. Appl. Supercond.* **32** 4000906
[63] Marchevsky M 2021 *Instruments* **5** 27 and references therein
[64] Takematsu T, Hu R, Takao T, Yanagisawa Y, Nakagome H, Uglietti D, Kiyoshi T, Takahashi M and Maeda H 2010 *Physica* C **470** 674–7
[65] Yanagisawa Y, Sato K, Piao R, Nakagome H, Takematsu T, Takao T, Kamibayashi H, Takahashi M and Maeda H 2012 *Physica* C **476** 19–22
[66] Barth C, Bagrets N, Weiss K-P, Bayer C M and Bast T 2013 *Supercond. Sci. Technol.* **26** 055007
[67] Otten S, Dhallé M, Gao P, Wessel W, Kario A, Kling A and Goldacker W 2015 *Supercond. Sci. Technol.* **28** 065014
[68] Talantsev E F, Badcock R A, Mataira R, Chong S V, Bouloukakis K, Hamilton K and Long N J 2017 *Supercond. Sci. Technol.* **30** 045014
[69] Kesgin I, Hasse Q, Ivanyushenkov Y and Welp U 2017 *IOP Conf. Ser.: Mater. Sci. Eng.* **279** 012009
[70] Gao P, Wessel W A J, Dhallé M, Otten S, Kario A, Van Nugteren J, Kirby G, Bottura L and ten Kate H H J 2019 *Supercond. Sci. Technol.* **32** 055006
[71] Yin S, Duranti M, Swenson C A, Li P, Ye L, Zhang X and Shen T 2020 *J. Appl. Phys.* **128** 173903
[72] Stern J, Swanson J, Bogdanof T, Krutulis M, Weiss J, van der Laan D, Wang X and Chiesa L 2022 *IEEE Trans. Appl. Supercond.* **32** 4800904
[73] Luo L, Ferracin P, Stern J, Van der Laan D, Wang X, Weiss J and Wu Y 2022 *IEEE Trans. Appl. Supercond.* **32** 9000906
[74] Scurti F, Ishmael S, Flanagan G and Schwartz J 2016 *Supercond. Sci. Technol.* **29** 03LT01
[75] Salazar E E *et al* 2021 *Supercond. Sci. Technol.* **34** 035027
[76] Lu J, Xin Y, Jarvis B and Bai H 2021 *Supercond. Sci. Technol.* **34** 075004
[77] Bonura M, Cayado P, Konstantopoulou K, Alessandrini M and Carmine S 2022 *ACS Appl. Electron. Mater.* **4** 1318–26
[78] Lacroix C, Sirois F and Lupien J H F 2017 *Supercond. Sci. Technol.* **30** 064004
[79] Rochepault E, Ferracin P and Vallone G 2022 *IEEE Trans. Appl. Supercond.* **32** 4003505
[80] Uglietti D, Kang R, Wesche R and Grilli F 2020 *Cryogenics* **110** 103118
[81] Pothavajhala V, Graber L, Kim C H and Pamidi S 2014 *IEEE Trans. Appl. Supercond.* **24** 4800505
[82] Araujo Martínez A C, Ji Q, Prestemon S O, Wang X and Maury Cuna G H I 2020 *IEEE Trans. Appl. Supercond.* **30** 6600605
[83] Teyber R, Marchevsky M, Araujo Martinez A C, Prestemon S, Weiss J D and van der Laan D C 2022 *Supercond. Sci. Technol.* **35** 094008
[84] ngspice (availble at: https://ngspice.sourceforge.io/index.html)
[85] Sammut N, Bottura L and Micallef J 2006 *Phys. Rev. ST Accel. Beams* **9** 012402